JOURNAL OF GUIDANCE, CONTROL, AND DYNAMICS
Vol. 33, No. 6, November–December 2010

Engineering Notes

Unmanned Aerial Vehicle Coordination on Closed Convex Paths in Wind

Laszlo Techy*
University of Washington, Seattle, Washington 98195
Derek A. Paley†
University of Maryland, College Park, Maryland 20742
and
Craig A. Woolsey‡
Virginia Polytechnic Institute and State University, Blacksburg, Virginia 24061

DOI: 10.2514/1.47655

I. Introduction

IN THIS Note we consider the problem of motion coordination of an aerial robotic network in the presence of steady, uniform winds. We present application examples of multivehicle coordination and path planning methods. The control laws we employ are extensions of previous research results on particle coordination and minimum-time path planning in steady, uniform wind. In prior work most relevant to this Note, Lyapunov-based control laws are provided to drive a collective of vehicles to a symmetric pattern along a circular orbit [1], to coordinated patterns on convex curves [2], and to coordinated patterns in the presence of winds [3]. The development of minimum-time path planning algorithms is also relevant [4,5].

The vehicle coordination framework described here may serve as an intermediate layer between low-level vehicle control and high-level mission planning. We assume that the control signal is the turn rate-of-change, which, in the case of a fixed-wing aircraft, may be controlled by regulating the bank angle. We also assume that the low-level controller (the autopilot) can execute the desired turn-rate commands. Similar vehicle models have been frequently used to design kinematic control laws to track targets with aerial vehicles [6–9]. Coordinated steering laws were presented in [10], where it was shown that collective motion along parallel lines or around the same circle are the only relative equilibria if the particle steering laws depend only on relative positions and headings. Motivated by the need for coordination on curves of arbitrary shapes, Lyapunov-based control laws were presented in [11], in which relative arc lengths between particles were used for coordination, as opposed to relative phases. Leader–follower approaches have also been studied (see, for example, [12,13] and the references therein).

Presented as Paper 2009-6210 at the AIAA Guidance, Navigation, and Control Conference, Chicago, IL, 10–13 August 2009; received 15 October 2009; revision received 11 July 2010; accepted for publication 12 July 2010.

*Research Associate, Aeronautics and Astronautics; techy@uw.edu. Member AIAA.

†Assistant Professor, Aerospace Engineering; dpaley@umd.edu. Senior Member AIAA.

‡Associate Professor, Aerospace and Ocean Engineering; cwoolsey@vt.edu. Associate Fellow AIAA.

The contributions of this Note are twofold: First, we extend an existing motion-coordination framework to the case in which the vehicles travel around strictly convex loops in the presence of a steady, uniform flowfield. Second, we present an approximation method that generates strictly convex curves from convex paths that may contain straight segments. The latter method is important to allow coordination on time-optimal paths, which frequently contain straight segments. This Note also includes simulation results focusing on two application examples: control-volume sampling and perimeter defense.

In Sec. II we describe the motion-coordination algorithms. In Sec. III we present the curve-approximation method that enables coordinated control on approximately time-optimal paths. In Secs. IV and V we describe the application examples. Section VI summarizes this Note.

II. Unmanned Aerial Vehicle Modeling and the Motion-Coordination Algorithm

We use a planar self-propelled particle model to describe the motion of unmanned aerial vehicles (UAVs) in ambient winds [3]. In this model, we assume that the particles are traveling at unit speed relative to a steady, uniform flowfield whose magnitude is strictly less than one. Identifying the complex plane with the plane of motion, we express the position of each particle by $r_k = x_k + iy_k$ and the flow-relative velocity of each particle by $e^{i\theta_k}$, where θ_k is the orientation of the flow-relative velocity. Let $\beta \in \mathbb{R}$ denote the magnitude of the ambient flow which we assume, without loss of generality, to be aligned with the real axis. The components x_k and y_k are expressed in an Earth-fixed inertial frame, where the x axis points to the north, the y axis points to the east, and the z axis points down. The equations of motion are

$$\dot{r}_k = e^{i\theta_k} + \beta \qquad \dot{\theta}_k = u_k \tag{1}$$

where u_k is the turn-rate control for the kth particle. In terms of the inertial speed s_k and course angle γ_k, Eq. (1) becomes [3]

$$\dot{r}_k = s_k e^{i\gamma_k} \qquad \dot{\gamma}_k = \nu_k \tag{2}$$

where ν_k may be taken as the input (see [3]).

For the control input $\nu_k = \kappa_0 s_k$, with $\kappa_0 = \text{const} \neq 0$, the particle k orbits a circle of radius $|1/\kappa_0|$ and with fixed center[§]:

$$c_k = r_k + (1/\kappa_0) i e^{i\gamma_k} \tag{3}$$

Indeed, along solutions of Eq. (2), $\dot{c}_k = (s_k - (1/\kappa_0)\nu_k)e^{i\gamma_k} \equiv 0$. If there is no ambient flow, then $s_k = s = 1$. Setting $\nu_k = \kappa_k s$, where κ_k is the curvature of a strictly convex loop C, drives the particle k around a curve C whose center c_k is fixed [2]. The main observation of this section is the following.

Proposition 1. For the model (2) with control input

$$\nu_k = \kappa_k s_k$$

particle k travels along the curve C with the curve center fixed in inertial space.

The proof is straightforward extension of Lemma 1 in [3] to convex curves. The significance of this observation is that it makes

[§]The center of the convex curve can be, in general, any fixed point inside the region enclosed by the curve that stays fixed with respect to the curve. For common geometrical shapes, such as circles and ellipses, analytical expression exists between the curve center and a point on the curve. (Also see [2].)

many prior results applicable to the problem of motion coordination on a convex loop in a flowfield.

As an example, we derive a decentralized control law that drives particle k around a strictly convex loop C with an arbitrary center c_0 fixed in inertial space. Let $\boldsymbol{r}$ and γ be the vectors of N particles' speeds s_k and course angles γ_k, respectively. Also define the vector $\mathbf{1} = [1, \ldots, 1]^T \in \mathbb{R}^N$ and let $\boldsymbol{c}$ be the vector of curve centers c_k relative to c_0 [1]. Define the potential function

$$S(\boldsymbol{r}, \gamma) = \frac{1}{2}\langle \boldsymbol{c}, P\boldsymbol{c}\rangle$$

where $P = \text{diag}\{\mathbf{1}\} - \frac{1}{N}\mathbf{1}\mathbf{1}^T$. The time derivative of $S(\boldsymbol{r}, \gamma)$ along the solutions of Eq. (2) is [2]

$$\dot{S}(\boldsymbol{r}, \boldsymbol{\gamma}) = \sum_{j=1}^{N}\langle \dot{c}_j, P_j\boldsymbol{c}\rangle = \sum_{j=1}^{N}\langle e^{i\gamma_j}, P_j\boldsymbol{c}\rangle(s_j - \kappa_j^{-1}v_j) \tag{4}$$

where P_j denotes the jth row of P. Choosing the control

$$v_k = \kappa_k(s_k + K_0\langle e^{i\gamma_k}, P_k\boldsymbol{c}\rangle), \qquad K_0 > 0 \tag{5}$$

forces all particles to travel around C. To prove this result, one may observe that $\dot{S} \leq 0$ and apply tools from Lyapunov stability theory [2].

It is possible to extend the control law to enforce convergence to the critical set of a phase potential, such that the particles are equally separated in time, as has been previously shown for circular formations in a steady flow [3]. This result relies on the notion of the *time phase*:

$$\psi_k = \frac{2\pi}{T}\int_0^{\gamma_k}\frac{d\gamma}{\kappa(\gamma)s(\gamma)} \tag{6}$$

where $T > 0$ is the period of a single orbit. Consider the composite potential

$$V(\boldsymbol{r}, \boldsymbol{\gamma}) = S(\boldsymbol{r}, \boldsymbol{\gamma}) + \frac{T}{2\pi}U(\boldsymbol{\psi}) \tag{7}$$

where $S(\boldsymbol{r}, \boldsymbol{\gamma}) = (1/2)\langle \boldsymbol{c}, P\boldsymbol{c}\rangle$ and $U(\boldsymbol{\psi})$ is a rotationally symmetric phase potential. Rotational symmetry of U implies

$$\sum_{j=1}^{N}\frac{\partial U}{\partial \psi_j} = 0$$

Along solutions of Eq. (2) we have

$$\dot{V} = \sum_{j=1}^{N}\left(s_j\langle e^{i\gamma_j}, P_j\boldsymbol{c}\rangle - \frac{\partial U}{\partial \psi_j}\right)(1 - (\kappa_j s_j)^{-1}v_j) \tag{8}$$

Choosing the control law

$$v_k = \kappa_k s_k\left(1 + K_0\left(s_k\langle e^{i\gamma_k}, P_k\boldsymbol{c}\rangle - \frac{\partial U}{\partial \psi_k}\right)\right), \qquad K_0 > 0 \tag{9}$$

enforces convergence of all particles to C with a phase arrangement in the critical set of U [1].

We coordinate the time phase on C by choosing $U(\boldsymbol{\psi})$ to be an (M, N) pattern potential [1]. An (M, N) pattern is a symmetric arrangement of phases consisting of M clusters, each with N/M particles, uniformly spaced around the curve. The (N, N) pattern is the so-called splay pattern, in which the time phases are uniformly separated: a *time-splay* formation [3].

III. Strictly Convex Approximation of Linear Segments

The UAV coordination algorithm described in Sec. II applies only to closed curves that are strictly convex: i.e., curves with nonzero curvature. In practical applications such as environmental sampling or perimeter patrol (discussed in Secs. IV and V, respectively), a desired path may contain linear segments. For example, minimum-time paths may contain singular arcs that correspond to rectilinear motion [4]. In this section, we provide a method for approximating a linear segment of a closed convex curve with a circular arc.

Consider a smooth (C^1) convex curve, regularly parameterized by t. A point on the path is denoted as $\eta(t)$. The vector tangent to that point is given by $\dot{\eta}(t)$, and in complex notation the normal is $i\dot{\eta}(t)$. As defined here, the normal points toward the interior of a closed convex path for clockwise motion around the path (see Fig. 1). Suppose the given path contains a single segment where the curvature is zero. Let t_α denote the path parameter value where the straight segment begins and let t_β denote the path parameter value where the segment ends. The lines defined by the normal vectors at t_α and t_β are parallel. As shown in the following lemma [14], though, for any specified $R_0 \in \mathbb{R}$ large enough, there exist small parameters t_α^ϵ and t_β^ϵ such that the lines normal to $\eta(t_\alpha - t_\alpha^\epsilon)$ and $\eta(t_\beta + t_\beta^\epsilon)$ intersect at a single point:

$$c = \eta(t_\alpha - t_\alpha^\epsilon) + R_0 i\dot{\eta}(t_\alpha - t_\alpha^\epsilon) = \eta(t_\beta + t_\beta^\epsilon) + R_0 i\dot{\eta}(t_\beta + t_\beta^\epsilon) \tag{10}$$

Lemma 1. Consider a closed C^1 convex curve $\eta(t)$ that is regularly parameterized by $t \in [t_0, t_0 + T]$ with $T > 0$ and with $\eta(t_0) = \eta(t_0 + T)$. Suppose this curve has a single linear segment such that

$$\kappa(t) = 0, \quad t \in (t_\alpha, t_\beta)$$

where $t_0 < t_\alpha < t_\beta < t_0 + T$. Elsewhere on the curve, the curvature is nonzero (and of constant sign). There exist values $t_\alpha^\epsilon \in (0, t_\alpha - t_0]$ and $t_\beta^\epsilon \in (0, t_0 + T - t_\beta]$ such that a circle of radius $R_0 > 0$ is tangent to the curve $\eta(t)$ at points $\eta(t_\alpha - t_\alpha^\epsilon)$ and $\eta(t_\beta + t_\beta^\epsilon)$. The radius R_0 can be chosen arbitrarily large.

Proof: Let $t_A = t_\alpha - t_\alpha^\epsilon$ and $t_B = t_\beta + t_\beta^\epsilon$. For t_α^ϵ and t_β^ϵ sufficiently small positive, the normals to $\eta(t_A)$ and $\eta(t_B)$ will intersect at some point $c = c(t_\alpha^\epsilon, t_\beta^\epsilon)$. Let

$$R_A(t_\alpha^\epsilon) = \|c - \eta(t_A)\| \quad \text{and} \quad R_B(t_\beta^\epsilon) = \|c - \eta(t_B)\|$$

For a given value $t_\alpha^\epsilon > 0$, sufficiently small, there exists $t_\beta^\epsilon > 0$ such that $R_A(t_\alpha^\epsilon) = R_B(t_\beta^\epsilon) = R_0 > 0$. To establish the existence of t_β^ϵ, define the continuous function $f(t_\beta^\epsilon) = R_A(t_\alpha^\epsilon) - R_B(t_\beta^\epsilon)$. Noting that $R_B(0) < R_A(t_\alpha^\epsilon)$, by continuity of $\eta(t)$ and $\dot{\eta}(t)$, it follows that $f(0) > 0$. By convexity of $\eta(t)$ there exists a value $\bar{t}_\beta^\epsilon$ such that the points $c(t_\alpha^\epsilon, \bar{t}_\beta^\epsilon)$ and $\eta(t_A)$ coincide. In this case, $R_A(t_\alpha^\epsilon) = 0$ and $R_B(\bar{t}_\beta^\epsilon) > 0$ so that $f(\bar{t}_\beta^\epsilon) = -R_B(\bar{t}_\beta^\epsilon) < 0$. By continuity of $f(\cdot)$ there must exist $t_\beta^\epsilon \in (0, \bar{t}_\beta^\epsilon)$ such that $f(t_\beta^\epsilon) = 0$. □

In practice, one may specify a large value of the radius R_0 and use a numerical algorithm to determine both t_α^ϵ and t_β^ϵ from Eq. (10). Figure 2 shows a path that was generated by a time-optimal planning algorithm [4]. The straight segment is approximated by circular arcs of radii $R_0 = 700$, 1000, and 2000 m, as shown on the right.

IV. Application Example 1: Control-Volume Sampling

In this section we present an environmental sampling problem, discussed in [5], that motivated some of the efforts described in this Note. Consider two UAVs tasked with measuring some atmospheric

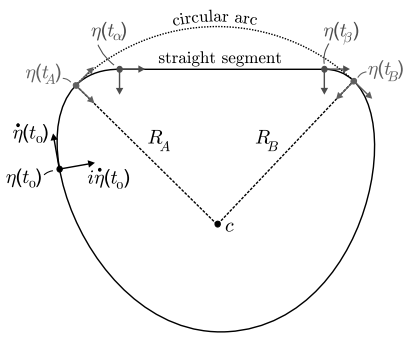

Fig. 1 Approximating a zero curvature segment with a circular arc.

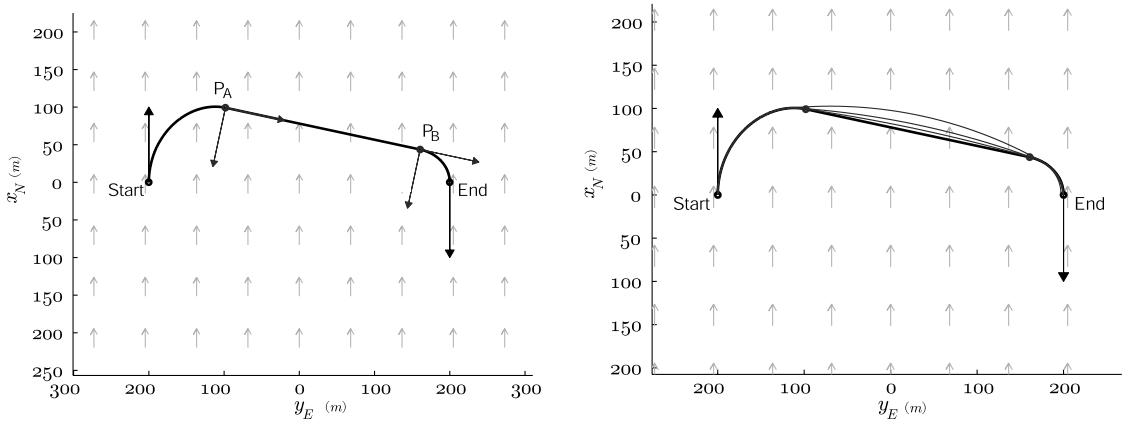

a) Minimum-time path between initial and final points **b) Approximating circular arcs**

Fig. 2 Straight portions of closed convex curves can be approximated by circular arcs to arbitrary precision.

constituent (particles, sporangia, volatile organic compounds, etc.) in a region that contains a source of this constituent. Of particular interest is the control-volume sampling scenario, in which one wishes to quantify the rate of release of the measured quantity within the control volume.

The control-volume equation for the rate-of-change of an extensive (scalar or vector) quantity $\boldsymbol{Q}$ in a *fixed* volume of interest is [15]

$$\iint_{CS} \frac{\mathrm{d}\boldsymbol{Q}}{\mathrm{d}V}\boldsymbol{V}\cdot\mathbf{d}\boldsymbol{A} + \frac{\partial}{\partial t}\iiint_{CV}\frac{\mathrm{d}\boldsymbol{Q}}{\mathrm{d}V}\,\mathrm{d}V = 0$$

The first term on the left accounts for the flow of the quantity across the control surface (the control-volume boundary) and the second term accounts for the rate-of-change of the property within the control volume (see Fig. 3a). Suppose $\boldsymbol{Q}$ represents the number of particles (e.g., plant pathogen spores) in the control volume. Then the first term on the left represents the net flux of particles out of the control volume and the second represents the rate at which particles are released within the volume.

One challenge in aerobiological sampling [5,14] is to estimate the source strength of an infected crop field as plant pathogen spores are released from the crop canopy. Measuring the net outflow across the boundaries of the control volume removes background disease from the measurement, allowing one to determine the rate of pathogen release within the control volume. In the framework summarized in this section, the outflow across the boundaries of the control volume is measured using two UAVs equipped with spore-collection devices that open and close in flight [5]. Based on the sample time and the measured airspeed, one may assess the average spore concentration; the samples from a given sampling flight provide a time-averaged measurement over the duration of that flight. Imagine the closed flight path to be separated into two equal length sections (e.g., two halves of a circle) with an imaginary dividing line: one section lies downwind from the source and one lies upwind. The difference in the average concentration measurements along these two arcs characterizes the net outflow across the boundaries, and thus the rate of spore release.

When the vehicles are not sampling, they reinitialize to begin the next sampling leg. Since the vehicles are not sampling during this period, they should reinitialize as quickly as possible to save time and fuel, increasing the total volume of air that is sampled. The idea is illustrated in Fig. 4, where the semicircular sampling arcs and connecting reinitialization paths are shown for both vehicles. The path planning algorithm of [4] yields the minimum-time trajectories for optimal reinitialization [5,14]. Because of its shape, we refer to the closed convex curve that results as a *D curve*. The vehicles coordinate their flight along these closed convex paths to ensure consistent sampling; during sampling intervals, one UAV is upwind and the other is downwind.

We note that the reinitialization interval assumes maximum control effort (maximum turn-rate), which constrains one's ability to enforce convergence to the path. In practice, the reinitialization path is generated with an artificial turn-rate limit that is strictly less than the true maximum turn rate. This ensures that the UAV is able to track the desired path even in the presence of disturbances.

A. Parametrization of D Curves

Let $\eta(t) \in \mathbb{C} \sim \mathbb{R}^2$ represent a smooth curve in the plane parameterized by the path parameter t. Such a curve can be uniquely described by specifying its curvature at any instant along the curve. The parametrization of the D curves is

$$\kappa(t) = \begin{cases} \frac{1+\beta(s(t)\cos\gamma(t)-\beta)}{s(t)^3}|u_{\max}| & t \in [0, t_\alpha - t_\alpha^\epsilon] \\ \frac{1}{R_0} & t \in [t_\alpha - t_\alpha^\epsilon, t_\beta + t_\beta^\epsilon] \\ \frac{1+\beta(s(t)\cos\gamma(t)-\beta)}{s(t)^3}|u_{\max}| & t \in [t_\beta + t_\beta^\epsilon, t_C] \\ \frac{1}{R} & t \in [t_C, T] \end{cases} \tag{11}$$

where $u_{\max}$ is the turn-rate limit used by the path generation algorithm to determine the time-optimal trajectory. (Note that *turn*

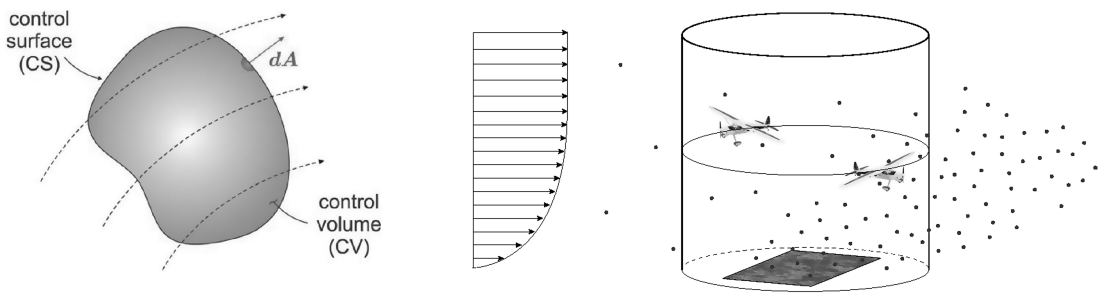

a) Illustration of a control volume in a flow **b) Particle flow in an aerobiological sampling problem**

Fig. 3 Net rate of outflow across the boundaries of the volume.

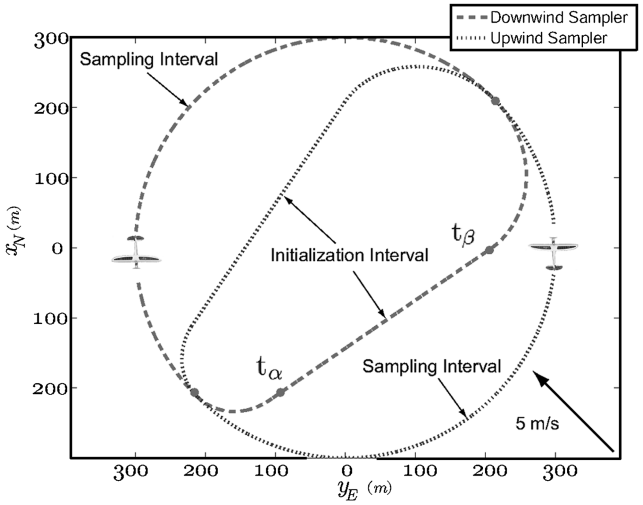

Fig. 4 Two UAVs flying in the control-volume sampling mission. UAV1 (UAV2) samples only during the upwind (downwind) path segment. The endpoints of the sampling arc are connected with a time-optimal path.

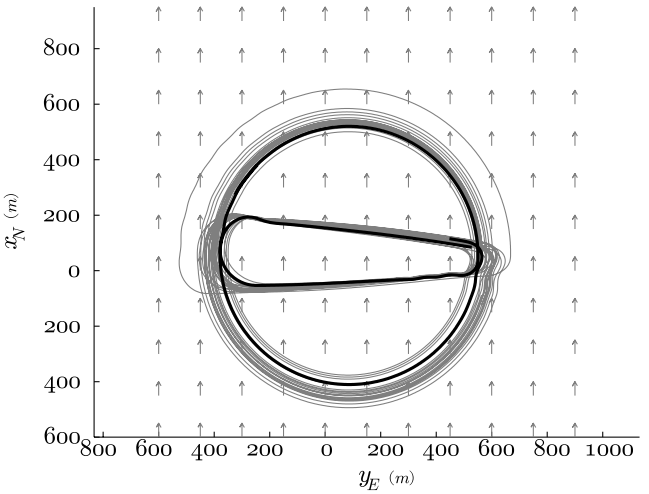

Fig. 5 Hardware-in-the-loop simulation results for the control-volume sampling problem. The figure shows simulation results over the course of a 45 min sampling. The bold line shows the last orbit.

rate refers to the vehicle's heading rate, as opposed to the course rate, which depends on the ambient flow.) In the above definition, the first and third entries correspond to maximum turn-rate segments, the second entry corresponds to a circular arc that approximates a straight segment, and the last entry corresponds to a circular segment with radius R. The first three entries correspond to the time-optimal reinitialization path, and the last entry corresponds to the sampling interval, where the radius of curvature is held constant for the duration of a semicircle.

B. Hardware-in-the-Loop Simulations

The proposed method has been implemented for real-time execution and tested in hardware-in-the-loop (HIL) simulations. The motion of the two UAVs was simulated on two separate PCs that provided simulated sensor and telemetry information to the autopilots. The autopilots received the simulated telemetry data and ensured stable wings-level or equilibrium turning flight. The telemetry information from the autopilot was also shared with two onboard UAV PC-104 computers over serial RS-232 link. The PC-104 computers were equipped with wireless mesh networking cards to share relative position and phase information that was necessary for the coordination algorithm. Based on these data the PC-104 computers calculated the desired turn-rate commands according to a coordinated control law [3,14]. The turn-rate commands were then sent to the autopilots for execution.

The coordination technique described in Sec. II was used to properly phase the vehicles. Note that in the setting of Sec. II the vehicles share the same closed curve, while in the control-volume sampling problem the curves are different. Because of the symmetry in the problem, however, the time required for the vehicles to complete a full period is the same for the upwind and downwind samplers; the period T for a single orbit is the same for both vehicles. This observation indicates rotational symmetry in the time phase. Initializing $t = 0$ for both vehicles at the instant they start their sampling interval ensures that the synchronized $(M, N) = (1, 2)$ pattern corresponds to the case in which both vehicles start and finish their sampling turn at the same time. The two UAVs are equally separated temporally, and this separation is conserved during the entire loop. Note that in this case the $(M, N) = (1, 2)$ pattern is equivalent to a splay state, because the UAVs do not share the same path.

The airspeed used in HIL simulations was $V_a = 20$ m/s and the wind speed was $V_w = 5$ m/s. The minimum-time paths were designed with the assumption that the maximum bank angle is $\phi_{\max} = 25°$. The radius of the circular sampling path was chosen as $R = 500$ m. Figure 5 shows the simulation results of the control-volume sampling over the course of a 45 min sampling mission. Although the UAVs track the desired path and coordinate their motion, we can see that the tracking of the desired path is not perfect. The points connecting the different segments around the path correspond to discontinuities in the path curvature. At such points the vehicles would need to change their turn rate instantaneously, which is not possible for fixed-wing aircraft. At these points a slight overshoot can be observed, which is then compensated by feedback.

V. Application Example 2: Coordinated Perimeter Patrol

In the previous section we considered an environmental sampling application. Here, we discuss the application of the motion-coordination algorithms for integrated base defense. Consider a convex perimeter circumscribing a base that must be defended by a collection of N UAVs [16]. We seek an optimal method for patrolling the perimeter *and* responding to intruder alerts along the perimeter, as summarized by the following two objectives:

1) In nominal conditions, the UAVs coordinate their motion along the perimeter such that the visitation rate at any given point along the curve is constant.

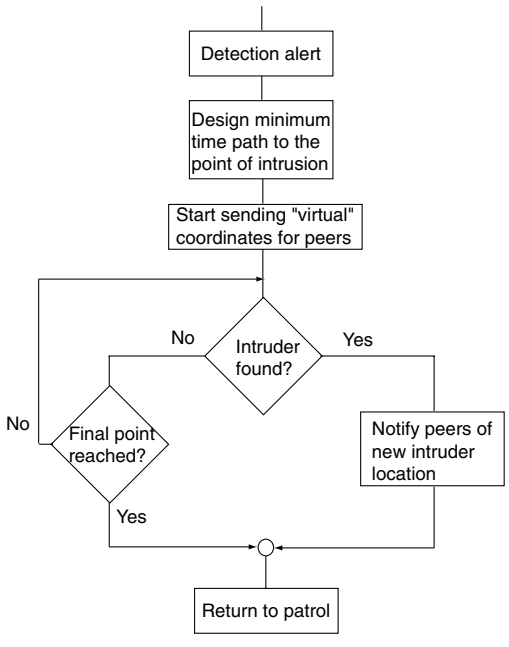

Fig. 6 Flow diagram of the time-optimal alert response scenario.

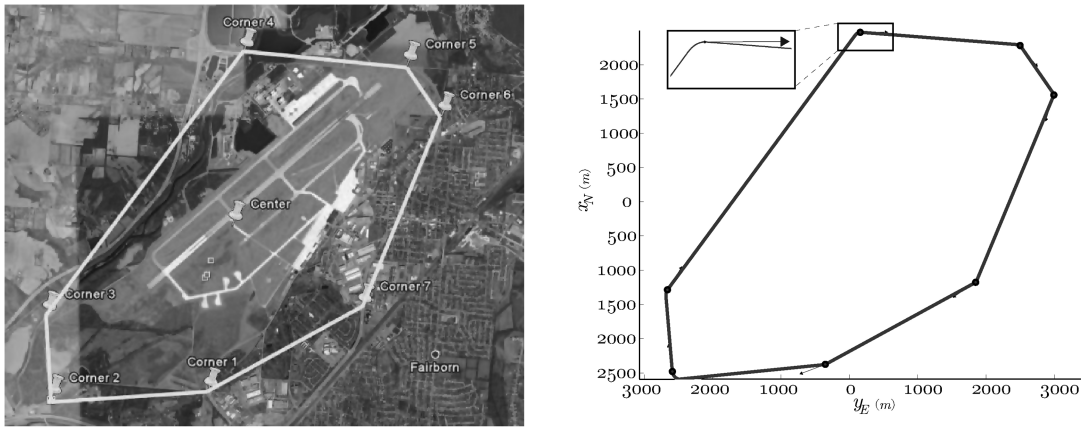

a) Satellite map of WPAFB **b) Strictly convex curve around WPAFB**

Fig. 7 Seven points were selected around WPAFB to define a closed convex curve. The curve then serves as the perimeter to be patrolled by a team of UAVs. The straight segments are approximated by arcs of circles of radius $R_0 = 50$ km. The arrows at the corner points in the right figure indicate the heading angle of the vehicle.

2) If an intruder is detected, one UAV responds in minimum time, while the remaining $N-1$ UAVs continue to patrol the original perimeter.

When a threat is detected, there is a tradeoff between these two objectives. In one limiting case, the UAVs do not take any action other than reporting the threat and continuing their original coordinated flight plan. In this case, only the perimeter patrol objective is achieved. Alternatively, one of the UAVs (e.g., the one that detected the threat) might divert from the perimeter and loiter above the threat. In this case, the number of vehicles covering the perimeter decreases to $N-1$ and gaps in the perimeter coverage increase.

We propose an approach to perimeter surveillance that balances the two objectives. Consider the event in which a threat is detected by one of the UAVs (UAV_1) at point r_f. The alert is reported to the rest of the group, and UAV_1 continues its flight path without diverting to investigate further. The next UAV in sequence (UAV_2) designs a minimum-time flight path from its current location to r_f and diverts from its original path to reach the threat as quickly as possible. (Here, we assume the threat is static, or slowly moving, relative to the intercept time for UAV_2.)

To ensure that the diversion of UAV_2 does not disrupt the remaining formation (and its perimeter surveillance task), the remaining $N-1$ UAVs assume that UAV_2 is continuing to maintain synchrony. Once the threat is detected again (or the endpoint of the time-optimal trajectory is reached, whichever occurs first), UAV_2 returns to the original flight plan. If UAV_2 confirms the threat, the next UAV in sequence (UAV_3) is tasked to arrive at the intrusion point in minimum time, and this cycle repeats. A flow diagram of the base-defense concept can be seen in Fig. 6.

The proposed framework has been tested in simulations. We selected the patrol perimeter to bound an existing establishment, Wright-Patterson Air Force Base (WPAFB). The base perimeter was defined by the convex hull of seven waypoints that were selected at landmarks around WPAFB. The points were selected at main road intersections, so that the nominal UAV paths follow main roads around the base. The wind speed was chosen to be $V_w = 10$ m/s from the south, and the airspeed of the UAVs was $V_a = 20$ m/s. A desired course angle was defined for each waypoint, based on the direction to the following waypoint. Time-optimal paths were defined between waypoints, as discussed in [4]. The resulting closed path is a convex curve with maximum rate turns at the curve corners. Figure 7a shows a satellite image of WPAFB with the seven selected waypoints around the base. Figure 7b shows the resulting closed strictly convex path to be followed.

The base perimeter was to be patrolled by $N = 4$ UAVs. An intrusion alert was simulated after all UAVs had converged to the desired time-splay arrangement, $(M, N) = (4, 4)$. The location of the intrusion point was at $[x_N, y_E]^T = [1300\text{ m}, -1250\text{ m}]^T$ (see Fig. 8a). After the intrusion was detected, the next UAV in line left the original patrol perimeter to fly to the intrusion point in minimum time (which was $T \approx 129$ s for the present simulation), as illustrated in Fig. 8b. While the UAV was following the minimum-time path to the intrusion location, its nominal position was shared with the rest of the group to ensure that the investigation did not disrupt the formation. After the prosecutor UAV reached the intruder location, it started the coordination algorithm again to converge back to the formation (Fig. 8c).

VI. Conclusions

This Note adapted a multi-UAV control algorithm for motion around strictly convex closed paths in steady, uniform wind. The control algorithm steers an arbitrary number of particles to a coordinated state in which all of the particles orbit the same strictly convex closed path. The temporal separation between particles is coordinated to be uniform and constant. If a desired path contains a straight segment, one may construct a circular arc that approximates this segment with arbitrary precision.

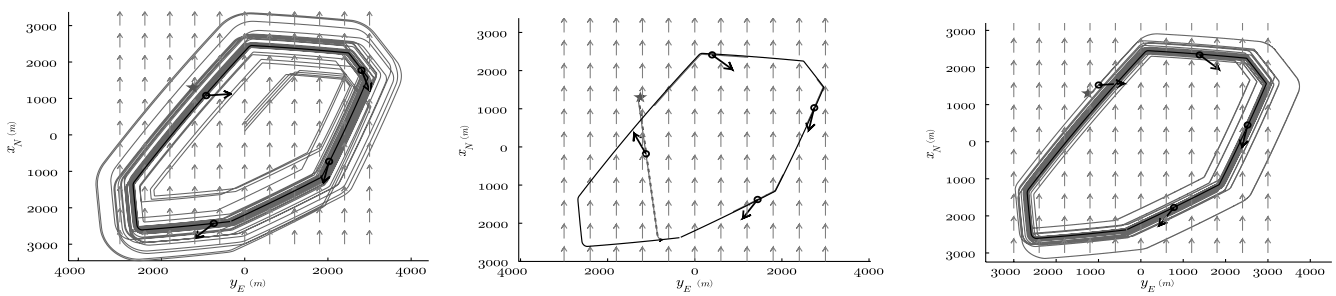

a) Time-splay coordination **b) Minimum-time alert response** **c) Returning to patrol**

Fig. 8 Simulation of coordinated perimeter coverage with time-optimal alert response around WPAFB.

This Note demonstrated the method's effectiveness for two examples: control-volume sampling and perimeter defense. In the control-volume sampling problem, two UAVs sample the air around the boundaries of a fixed volume to estimate the net rate of outflow of particles across the boundaries. The measurements can be used to estimate the rate of release of particles inside the control volume. Such measurements are important in aerobiological research, for example, to determine the rate at which pathogenic sporangia are released within a given area. In such a scenario the UAVs can synchronize their motion to perform consistent sampling during the mission.

In the integrated perimeter defense application, a team of UAVs is tasked with patrolling a convex perimeter such that the average visitation frequency at any given point along the perimeter is fixed and minimum. In the event of an intruder detection, a designated UAV follows a (nearly) time-optimal path to the location, while the remaining UAVs maintain the coordinated patrol. The algorithm represents a tradeoff between the competing objectives of consistent perimeter surveillance and rapid prosecution of an intruder alert.

Acknowledgments

This work was supported in part by the U.S. Office of Naval Research under grant nos. N00014-08-1-0012, N00014-10-1-0022, and N00014-09-1-1058. This material is also based upon work supported by the National Science Foundation under grant no. CMMI0928416.

References

[1] Sepulchre, R., Paley, D. A., and Leonard, N. E., "Stabilization of Planar Collective Motion: All-to-All Communication," *IEEE Transactions on Automatic Control*, Vol. 52, No. 5, 2007, pp. 811–824. doi:10.1109/TAC.2007.898077

[2] Paley, D. A., Leonard, N. E., and Sepulchre, R., "Stabilization of Symmetric Formations to Motion Around Convex Loops," *Systems and Control Letters*, Vol. 57, No. 3, March 2008, pp. 209–215. doi:10.1016/j.sysconle.2007.08.005

[3] Paley, D. A., and Peterson, C., "Stabilization of Collective Motion in a Time-Invariant Flowfield," *Journal of Guidance, Control, and Dynamics*, Vol. 32, No. 3, 2009, pp. 771–779. doi:10.2514/1.40636

[4] Techy, L., and Woolsey, C. A., "Minimum-Time Path Planning for Unmanned Aerial Vehicles in Steady Uniform Winds," *Journal of Guidance, Control, and Dynamics*, Vol. 32, No. 6, 2009, pp. 1736–1746. doi:10.2514/1.44580

[5] Techy, L., Woolsey, C. A., and Schmale, D. G., III, "Path Planning for Efficient UAV Coordination in Aerobiological Sampling Missions," *Proceedings of the 47th IEEE Conference on Decision and Control*, Inst. of Electrical and Electronics Engineers, Piscataway, NJ, Dec. 2008, pp. 2814–2819.

[6] Rysdyk, R. T., "Unmanned Aerial Vehicle Path Following and Target Observation in Wind," *Journal of Guidance, Control, and Dynamics*, Vol. 29, No. 5, 2006, pp. 1092–1100. doi:10.2514/1.19101

[7] Rysdyk, R. T., Lum, C., and Vagners, J., "Autonomous Orbit Coordination for Two Unmanned Aerial Vehicles," AIAA Guidance Navigation and Control Conference and Exhibit, AIAA Paper 2005-6362, San Francisco, Aug. 2005.

[8] Frew, E. W., Lawrence, D. A., and Morris, S., "Coordinated Standoff Tracking of Moving Targets Using Lyapunov Guidance Vector Fields," *Journal of Guidance, Control, and Dynamics*, Vol. 31, No. 2, 2008, pp. 290–306. doi:10.2514/1.30507

[9] Klein, D. J., and Morgansen, K. A., "Controlled Collective Motion for Trajectory Tracking," *Proceedings of the American Control Conference*, Inst. of Electrical and Electronics Engineers, Piscataway, NJ, June 2006.

[10] Justh, E. W., and Krishnaprasad, P. S., "Equilibria and Steering Laws for Planar Formations," *Systems and Control Letters*, Vol. 52, 2004, pp. 25–38. doi:10.1016/j.sysconle.2003.10.004

[11] Zhang, F. and Leonard, N. E., "Coordinated Patterns of Unit Speed Particles on a Closed Curve," *Systems and Control Letters*, Vol. 56, 2007, pp. 397–407. doi:10.1016/j.sysconle.2006.10.027

[12] Tanner, H. G., Kumar, V., and Pappas, G. J., "Leader-to-Formation Stability," *IEEE Transactions on Robotics and Automation*, Vol. 20, No. 3, June 2004, pp. 443–455. doi:10.1109/TRA.2004.825275

[13] Desai, J., Ostrowski, J., and Kumar, V., "Modeling and Control of Formations of Nonholonomic Mobile Robots," *IEEE Transactions on Robotics and Automation*, Vol. 17, No. 6, Dec. 2001, pp. 905–908. doi:10.1109/70.976023

[14] Techy, L., Paley, D. A., and Woolsey, C. A., "UAV Coordination on Convex Curves in Wind: An Environmental Sampling Application," *European Control Conference*, Budapest, 2009, pp. 4967–4972.

[15] White, F. M., *Viscous Fluid Flow*, McGraw-Hill, Inc., New York, NY, 2nd ed., 1991.

[16] Paley, D. A., Techy, L., and Woolsey, C. A., "Coordinated Perimeter Patrol with Minimum-Time Alert Response," AIAA Guidance, Navigation, and Control Conference, AIAA Paper 2009-6210, Chicago, 2009.